Contents lists available at ScienceDirect

Materials Science & Engineering C

journal homepage: www.elsevier.com/locate/msec

Tailoring the multiscale architecture of electrospun membranes to promote 3D cellular infiltration

Alexandre Morel [a,b,1], Anne Géraldine Guex [a,c,*,1], Fabian Itel [a], Sebastian Domaschke [d,e], Alexander E. Ehret [d,e], Stephen J. Ferguson [b], Giuseppino Fortunato [a,2], René M. Rossi [a,**]

[a] Empa, Swiss Federal Laboratories for Materials Science and Technology, Laboratory for Biomimetic Membranes and Textiles, 9014 St. Gallen, Switzerland
[b] Institute for Biomechanics, Department of Health Sciences and Technology, ETH Zürich, 8092 Zürich, Switzerland
[c] Empa, Swiss Federal Laboratories for Materials Science and Technology, Laboratory for Biointerfaces, 9014 St. Gallen, Switzerland
[d] Institute for Mechanical Systems, Department of Mechanical and Process Engineering, ETH Zürich, 8092 Zürich, Switzerland
[e] Empa, Swiss Federal Laboratories for Materials Science and Technology, Experimental Continuum Mechanics, 8600 Dübendorf, Switzerland

ARTICLE INFO

ABSTRACT

Controlling the architecture of engineered scaffolds is of outmost importance to induce a targeted cell response and ultimately achieve successful tissue regeneration upon implantation. Robust, reliable and reproducible methods to control scaffold properties at different levels are timely and highly important. However, the multi-scale architectural properties of electrospun membranes are very complex, in particular the role of fiber-to-fiber interactions on mechanical properties, and their effect on cell response remain largely unexplored. The work reported here reveals that the macroscopic membrane stiffness, observed by stress-strain curves, cannot be predicted solely based on the Young's moduli of the constituting fibers but is rather influenced by interactions on the microscale, namely the number of fiber-to-fiber bonds. To specifically control the formation of these bonds, solvent systems of the electrospinning solution were fine-tuned, affecting the membrane properties at every length-scale investigated. In contrast to dichloromethane that is characterized by a high vapor pressure, the use of trifluoroacetic acid, a solvent with a lower vapor pressure, favors the generation of fiber-to-fiber bonds. This ultimately led to an overall increased Young's modulus and yield stress of the membrane despite a lower stiffness of the constituting fibers. With respect to tissue engineering applications, an experimental setup was developed to investigate the effect of architectural parameters on the ability of cells to infiltrate and migrate within the scaffold. The results reveal that differences in fiber-to-fiber bonds significantly affect the infiltration of normal human dermal fibroblasts into the membranes. Membranes of loose fibers with low numbers of fiber-to-fiber bonds, as obtained from spinning solutions using dichloromethane, promote cellular infiltration and are thus promising candidates for the formation of a 3D tissue.

1. Introduction

Health concerns, economic and social challenges affecting our ageing society raise an urgent need for efficient, low-cost medical solutions [1]. In the field of tissue engineering and regenerative medicine, the development of advanced bone substitutes [2], artificial skin [3], or vascular grafts [4] gained tremendous interest to address diseases such as osteoporosis, diabetic foot ulcers, or cardiovascular diseases. Such in vitro engineered artificial tissues require substrates that can support the regeneration, repair and replacement of human native tissues [5]. In this regard, electrospinning has emerged as a very promising tool for cost-effective fabrication of scaffolds [6]. Indeed, electrospun membranes are praised for their high porosity, good pore interconnectivity and their architectural resemblance with the fibrous collagen/elastin network found in the extracellular matrix (ECM) [7]. These characteristics favor the diffusion of nutrients and oxygen within the entire scaffold volume,

---

which are essential to promote cell proliferation and differentiation. Nevertheless, the relatively small pore sizes of nanofibrous membranes remain a limiting factor for cellular infiltration and tissue ingrowth. This drawback has been partially addressed by employing specialized methods to obtain larger pore sizes, e.g. by use of thick micron-scaled fibers, by removal of sacrificial fibers or by cryogenic electrospinning [8–13]. Furthermore, the analysis of cell migration through electrospun membranes still lacks appropriate experimental setups and easy to use systems.

The mechanical properties of scaffolds are important parameters for successful integration in the host and should closely mimic the one of the targeted native tissue to ensure mechanical stability and appropriate cell response [14–16]. Scaffold design should therefore consider the particular mechanical properties exhibited by the electrospun fibers and their membranes, compared to bulk-like polymeric materials [17–19]. Here, specific characteristics of the electrospinning fiber formation process come into play. For instance, a drastic increase in the fiber's Young's modulus E_f is observed for decreasing fiber diameters [20–23]. Moreover, the properties of the spinning polymer solutions such as the solvent volatility, polymer/solvent ratio, or polymer/solvent interaction also alter the resulting fiber properties [24,25]. Our previous study showed that a solvent with high vapor pressure and thus higher evaporation rate (e.g. dichloromethane, DCM) favored the formation of fibrillar structures at the surface of poly(L-lactide) (PLLA) fibers, which, in turn, enhanced the Young's modulus of individual fibers. On the other hand, solvents with lower evaporation rate, such as trifluoroacetic acid (TFA) promoted the formation of repetitive stacked lamellae, resulting in fibers with lower mechanical properties [26].

The fiber-to-fiber bonds also have an important role on the mechanical properties of electrospun membranes since they transmit the forces between fibers of the network. For instance, the Young's modulus E_m and tensile strength of polycaprolactone (PCL) membranes were enhanced by welding fibers at their cross-points through solvent vapor post-treatment [27]. The use of solvents with low vapor pressure is also known to favor the formation of welded cross-points due to the deposition of partially wet fibers during electrospinning [28,29]. However, for fiber-to-fiber junctions without clear welding, the nature of the adhesive forces is difficult to characterize. For instance, van der Waals forces were found to be the dominant attractive forces when contacting two individual PCL electrospun fibers [30,31]. Furthermore, the influence of electrospinning parameters on the formation and the nature of the generated fiber-to-fiber interactions has only been investigated in few studies [32–34]. For example, it was reported that fiber crossing points in poly(ester urethane) urea electrospun membranes were well bonded and that an increased number of these bonds correlated with increased mechanical anisotropy of the membranes despite almost constant fiber alignment. Additionally, the electrospinning methods were adjusted to tailor the mechanical properties of electrospun membranes by specifically tuning fiber alignment and fiber interconnections to address distinct tissue properties at the micro- or macro-scale.

The choice of an appropriate polymer is another crucial parameter for the fabrication of tissue engineering scaffolds since mechanical properties should match the destination tissue and chemical properties should favor cell-material interactions. Among other poly-esters, PLLA has been widely used in biomedical applications due to its biodegradability and cytocompatibility, and has gained increasing interest for the development of artificial tissues [35,36]. However, the ability to tailor the mechanical properties of electrospun membranes is limited due to their complex multiscale architectures and fiber-to-fiber interactions. In this study, we aimed at tailoring the fiber-to-fiber interactions at their crossing points by adjusting the spinning solution formulations. Namely, we elucidated how solvents of distinct volatility can either favor loose fiber-to-fiber junctions or induce the formation of physically bonded fibers (fiber-to-fiber bonds), without altering the overall architectural properties of the membranes. We thereby highlight how two visually comparable membranes reveal very different mechanical behavior.

PLLA membranes produced from DCM or TFA, respectively, were characterized with respect to their architectural as well as mechanical properties, both on the microscopic and macroscopic level. Individual fibers were defined in terms of diameter, straightness/tortuosity, and Young's modulus. The density of fiber-to-fiber bonds was studied by qualitatively visualizing the deformations of the fiber networks upon mechanical stretching, in particular the magnitude of the auxetic behavior [37]. On the macroscopic level, membranes were characterized based on porosity and fiber orientation, and analyzed based on stress-strain curves from uniaxial tensile testing.

To ultimately address differences on the cell or tissue level in biomedical application, local cell-fiber interactions need to be addressed and specific methods developed to study such interactions at different levels. The influence of different membrane properties, e.g. fiber-to-fiber bonds, porosity and fiber diameter, were thus evaluated in cell cultures of human dermal fibroblasts. Cell metabolic activity as well as migration through the membranes was assessed. We demonstrated that loose fiber-to-fiber junctions can be engineered to promote cell infiltration within the membrane. In summary, our results underline the importance of considering mechanical properties on the micro- and macro scale, in particular fiber-to-fiber bonds to explain whole membrane characteristics. These results contribute to a better understanding on how electrospinning parameters can be adjusted to tailor cell migration.

2. Materials and methods

2.1. Electrospinning

PLLA pellets were purchased from Natureworks (3100HP, containing <2% D-isomers). Dichloromethane (DCM) (Macron), trifluoroacetic acid (TFA) (ABCR) and dimethylformamide (DMF) (VWR Chemicals) were used to prepare two tailored electrospinning solutions. To investigate mechanical and architectural properties, the first solution (DCM90) was prepared in a 90/10 v/v DCM/DMF solvent mixture with a PLLA concentration of 9 wt% (9 g PLLA in 100 g solvent). The electrical conductivity of the solution was enhanced by the addition of tetraethylammonium bromide salt (TEAB, Sigma Aldrich) (300 mg TEAB in 100 g of solvent). The second solution (TFA100) was prepared at a concentration of 12 wt% PLLA in TFA (12 g PLLA in 100 g solvent). For cell infiltration experiments, two additional solutions were prepared in order to obtain slightly thicker fibers. The PLLA concentrations were increased to 12 wt% for the first solution (DCM90+) and to 14 wt% (TFA100+) for the second one, respectively.

A 3 ml plastic syringe containing the polymer solution was equipped with a blunt needle (0.8 mm inner diameter). The syringe pump (Aladin 1000, WPI) was set to deliver the solution at a flow rate of 16 µL·min^{-1}. A planar stainless-steel collector covered with parchment paper (BRANOPAC CZ) was placed in front of the needle at a distance of 15 cm, and a voltage of 15 kV was applied between both components. The relative humidity and temperature were set to 17% ($\pm$3%) and 21 °C ($\pm$1 °C), respectively. The obtained membranes were placed in a vacuum chamber for 1 h to remove any residual solvent. Evaporation properties of the two different solvents were simulated using Hansen Solubility Parameters in Practice (HSPiP) (http://www.hansen-solubility.com/) and presented in Fig. S1.

2.2. Fiber morphology and shape

The fiber morphology was visualized by scanning electron microscopy (SEM, Hitachi s-4800, Hitachi High-Technologies Corporation) with an acceleration voltage of 2 kV and a current flow of 10 µA. Beforehand, the samples were coated with an 8 nm thick gold palladium layer using a sputter coater (Leica EM ACE600, Leica Microsystems). ImageJ software was used for the measurement of the fiber diameter d_f ($n = 75$ per sample) based on SEM images [38].

In order to compare the straightness/tortuosity of the fibers forming

the different membranes, the fiber persistence length l_p was measured, a shape parameter introduced for the worm-like chain theory [39]. For this purpose, Easyworm software was used to trace segments of fibers ($n = 20$ per sample) based on SEM images [40]. The persistence length l_p was obtained from the mean square of the end-to-end distance $\langle R^2 \rangle$ of the traced segment and the segment arc length s according to the theoretical relation [41]

$$\langle R^2 \rangle = 4\, s\, l_\mathrm{p} \left[1 - 2\frac{l_\mathrm{p}}{s}\left(1 - e^{-\frac{s}{2l_\mathrm{p}}}\right)\right] \tag{1}$$

2.3. Membrane porosity and pore size

The thickness t_m of the membrane at the central region was measured using a profiler (Dektak 150, Veeco) equipped with a tip of 2.5 μm height ($n = 5$ measurements per membrane). The fiber content ν_F and overall porosity ϕ of the membrane were calculated from the thickness t_m, the area A and the mass m_m (weighing scale AT201, Mettler Toledo) of a cut sample, and the mass density $\rho = 1.25$ g cm^{-3} of PLLA according to [42–44]

$$\phi = 1 - \nu_\mathrm{F} = 1 - \frac{m_\mathrm{m}}{\rho\, t_\mathrm{m} A}. \tag{2}$$

The pore size was additionally estimated from SEM images using ImageJ software, where pores were defined as the polygonal areas comprised between neighboring fibers. As a selection criterion, the fibers visible inside the area should not be directly in contact with the fibers bordering the area, but ideally be located a few layers below them.

2.4. Uniaxial tensile testing

The uniaxial tensile experiment was described in a previous study [37]. Briefly, tests were carried out in triplicates ($n = 3$) with a custom-built set up. Samples with a width w_m of 10 mm were cut from the electrospun membranes and mounted horizontally on two clamps separated by 60 mm. The grip of the clamps was enhanced with sandpaper. Marker dots were drawn on the samples with a pen and recorded throughout the sample deformation with a camera (Pike F—100B Allied Vision Technologies GmbH) equipped with a 0.25× telecentric lens (TECHSPEC®, GoldTL™, Edmund Optics) to extract the local strain. The clamp displacement rate was set so that a nominal strain rate of 0.1% s^{-1} was achieved, and the force was recorded at 10 Hz by two 100 N force sensors (MTS Systems). The stress-strain plot was generated by post-processing the obtained data [45]. The nominal stress P

$$P = \frac{f}{t_\mathrm{m} w_\mathrm{m}} \tag{3}$$

was calculated from the force f and the initial cross-sectional area $t_\mathrm{m} w_\mathrm{m}$ of the sample. The Young's moduli E_m were determined as the slope of the lines fitted between 0.5% and 1% local strain of the stress-strain curves. Membrane thickness was measured as described above (Section 2.3).

2.5. SEM Imaging of network deformation

A custom-built stage was used to uniaxially stretch electrospun samples at defined global strains and to allow the visualization of the fiber networks by SEM without releasing the membrane from the stage. Samples with a width of 6 mm were fixed on clamps separated by 30 mm. Then, the clamps were moved manually to selected positions with a gear system, stretching the specimen to the predefined strain state. 20% global strain was selected for both top-view and side-view imaging. A gold palladium coating (thickness: 10 nm) was applied on the stretched samples and the stage was inserted in the SEM chamber to acquire images with an acceleration voltage of 2 kV and a current flow of 10 μA.

Duplicates were employed for each strain value. Side-view images were employed to measure the thickness of the membranes at 20% strain using ImageJ. Top-view images were used to qualitatively analyze the buckling amplitude of fibers caused by the lateral contraction of the membrane upon stretching.

2.6. Cell culture

In vitro cell experiments were carried out with normal human dermal fibroblasts (NHDF, female, Caucasian, skin/temple, C-29910, Promo-Cell, Germany) at passages 8 to12. The medium used for cell expansion and experiments was Dulbecco's modified Eagle's Medium (DMEM), high glucose (Sigma) with 10% fetal calf serum (FCS), 1% glutamine and 1% penicillin/streptomycin/neomycin. Incubation was set to 37 °C and 5% CO_2 in a humidified environment. Cells were trypsinized at 90% confluency for cell experiments or further passaging and culture.

2.7. Cell viability on PLLA membranes

Cell culture on electrospun membranes was carried out as previously established and reported [46]. In brief, samples of 4 mm in diameter were cut out using biopsy punches and fixed with insect pins in cell culture wells that were previously coated with a layer of cured poly-dimethylsiloxane (PDMS Sylgard 184, Sutter Kunststoffe). The samples were then sterilized under UV light in a cell culture hood for 30 min. NHDF were harvested and resuspended in complete medium. 10′000 NHDF in a volume of 30 μL were placed on top of the membranes and two hours after seeding, the wells were filled with media. AlamarBlue assays (Life Technologies, Thermo Fisher Scientific) were performed on day 1, 4, and 7 after seeding to assess the cell metabolic activity, indicative for cell viability. For these assays, NHDF were incubated for 2 h at 37 °C in 150 μL 10% (v/v) alamarBlue in phenol red free medium. 100 μL were then transferred to a new 96-well plate. AlamarBlue reduction was measured by fluorescence using an excitation wavelength $\lambda_\mathrm{ex} = 540$ nm and emission at $\lambda_\mathrm{em} = 580$ nm (Mithras2 Plate reader, Berthold Technologies). Measurements of samples incubated without cells were used for background correction. Cell metabolic activity was assessed in $N = 3$ individual experiments with $n = 3$ repeats in each condition.

For fluorescence microscopy, NDHF were fixed in 4% (v/v) formaldehyde in PBS, permeabilized in 0.1% (v/v) Triton™ X-100, and stained with Alexa®-546-conjugated phalloidin (~0.03 μM in PBS, Invitrogen, ThermoFisher Scientific). Nuclei were stained with 4′,6-diamidino-2-phenylindole (DAPI, 1 μg·mL^{-1} in PBS, Life Technologies, Thermo Fisher Scientific).

2.8. Cell sandwich culture

To assess cell migration through the fibrous structure, electrospun membranes were cut into circular pieces of 1 cm diameter and placed into 24 well-plates previously covered with a layer of PDMS. This membrane formed the first layer "*I*" of the sandwich (Fig. 1). A second membrane "*II*" was attached to the flat surface of a hollow glass cloning cylinder (8 mm inner Ø, Pyrex®, Sigma) using a thin layer of vacuum grease applied on the edge of the glass (Dow Corning® silicone high vacuum grease). Then, all membranes were UV-sterilized. Subsequently, while the cylinders were immersed in PBS at 37 °C to pre-wet the attached membranes *II*, 5×10^5 cells were seeded onto each membrane *I* in the wells. 24 h after seeding, media was removed and the membrane *II* /cylinder constructs were placed on top of the cells, such that the latter were sandwiched between the two membranes and the construct was then incubated for 18 days in cell medium. $N = 2$ individual experiments with $n = 3$ technical repeats for each condition were performed.
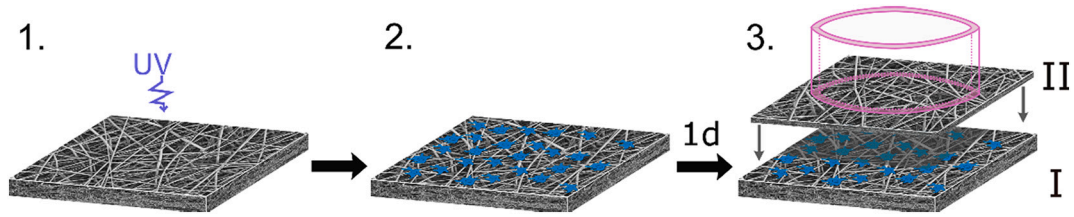
Fig. 1. Preparation of the cell sandwich experiment. 1. UV-sterilization of the membranes. 2. Seeding of NHDF (blue) on the bottom membrane *I*. 3. After 24 h, the membrane *II,* attached to a glass cylinder (purple) is added on top of the cells. Cell culture wells and cylinder were then filled separately with culture media to immerse both membranes. (For interpretation of the references to colour in this figure legend, the reader is referred to the web version of this article.)

2.9. Cell SEM imaging and analysis

The membranes *II* were fixed in 4% formaldehyde while being still attached to the cloning cylinder and subsequently dried in a series of increasing ethanol concentrations ranging from 30% up to 100% (30–60 min per step). Finally, hexamethyldisilazane (HMDS, Sigma) was added to the membranes for 5 min to remove remaining water, before samples were let to dry overnight. SEM images were acquired as described above (Section 2.2).

For the cell sandwich experiment, SEM pictures were used to measure the percentage of cell coverage on the surface of the top membrane *II*. This is a quantitative indicator of the cell migration and infiltration. For this purpose, maximal and minimal pixel intensities were adjusted to increase the contrast between the cells and the fiber network using ImageJ. Images were then smoothened and saved to PNG form. Binary segmentations were performed on the PNGs. Noise from the fiber network whose contrast with the cells was too low to be discriminated by the binary segmentation was reduced by removing signals smaller than 3 μm. Finally, the percentage of white and black was measured, representative for cell coverage.

2.10. Data processing and statistical analysis

Number of technical repeats and individual experiments are described under the respective sections. For low sample sizes (cell metabolic activity), no normal distribution was assumed and differences between the groups were assessed in a non-parametric Kruskal-Wallis test, followed by pairwise comparison in a Dunn's test. For larger sample sizes of 20 or more (fiber diameter), normal distribution was assumed and statistical difference between the groups assessed in an ANOVA test with Bonferroni correction. Statistically significant differences were considered for $P < 0.05$.

Experiments were performed with one electrospun membrane of each respective type (DCM90, TFA100, DCM90+, TFA100+). We therefore refrained from statistical analysis on membrane characterization due to the small sample size. For increased accuracy, measurements of thickness and area were performed five times and the resulting porosity calculated based on these measurements. To estimate the errors in the determined membrane's fiber density $\Delta\nu_F$ (and thus porosity $\Delta\phi$), a propagation of error analysis was performed, which is represented by

$$\frac{\Delta\nu_F}{\nu_F} = \frac{1}{\nu_F}\sqrt{\left(\frac{\partial\nu_F}{\partial m_m}\Delta m_m\right)^2 + \left(\frac{\partial\nu_F}{\partial t_m}\Delta t_m\right)^2 + \left(\frac{\partial\nu_F}{\partial A}\Delta A\right)^2} \quad (4)$$

and results in

$$\frac{\Delta\nu_F}{\nu_F} = \sqrt{\left(\frac{\Delta m_m}{m_m}\right)^2 + \left(\frac{\Delta t_m}{t_m}\right)^2 + \left(\frac{\Delta A}{A}\right)^2}, \quad (5)$$

where in Eq. (5) $\frac{\Delta m_m}{m_m}$ (=3%) was evaluated based on the scale's accuracy, $\frac{\Delta A}{A}$ (=2%) calculated from the deviations when measuring the same area five times ($n = 5$) and Δt_m from the deviations calculated for the thickness measurements.

3. Results and discussion

Electrospun membranes experience an incessant popularity as cell culture substrates for tissue engineering applications and bring along a plethora of parameters to characterize and fine-tune. Here, we are addressing the importance of fiber-to-fiber interactions within electrospun membranes and discuss how they can be tailored by specific solvent systems, i.e. by using DCM or TFA-based spinning solutions. Specifically, we provide evidence that standard SEM imaging cannot be used to assess the nature and number of fiber-to-fiber interactions as two membranes that are visually comparable can incorporate either loose junctions or physical bonds between fibers. To address this issue, we elaborate on methods to characterize fiber-to-fiber bonds based on their auxetic behavior upon lateral stretching. This new approach reveals that the overall Young's modulus of membranes does not directly correlate with the Young's modulus of individual fibers but is also governed by fiber-to-fiber bonds. Ultimately, we show that fiber-to-fiber interactions and resulting "loose" or "bonded" fibrous networks influence cell migration.

3.1. Single fiber characterization and resulting membrane properties

Representing the construction unit of electrospun membranes, the single fiber needs to be thoroughly characterized with respect to its morphological and mechanical characteristics. This allows one to assess its contribution to the mechanical properties of the whole membrane and thus the influence on cell response. SEM images of DCM90 and TFA100 membranes revealed homogenous, smooth fibers of both membranes (Fig. 2). Electrospinning solutions and parameters were tailored to obtain similar fiber diameters, which were 390 ± 90 nm for the DCM90 mesh and 460 ± 100 nm for the TFA100 membrane, respectively. Despite a similar range, statistical analysis revealed a significant difference between the mean fiber diameter of the membranes. With a difference of 17% we consider that the fiber diameters are still within the same orders of magnitude. To assess the fiber straightness, the persistence lengths l_p of fiber segments was measured, as this parameter describes the distance along the fiber over which correlations in the direction of the tangent are lost. For both samples l_p was found in a similar range, with 558 ± 200 μm for the DCM90 sample and 473 ± 160 μm for the TFA100 one. These parameters (d_f and l_p) are considered as two of the predominant factors for the mechanical properties of electrospun membranes [47–49].

Another important characteristic of fibers is their Young's moduli E_f. In our previous work [26], E_f of DCM90 and TFA100 single fibers were measured by AFM-based three-point-bending tests. For better comparison with the here obtained data, the trend lines of the results of these experiments are reported in Fig. 3A. They revealed that for the same fiber diameter, the Young's modulus of DCM90 single fibers was higher than for TFA100 fibers. The difference in mechanical properties between the fibers was attributed to their respective internal structure. While DCM90 fibers incorporated parallel nanofibrils oriented along the fibers' axis, TFA100 fibers presented more relaxed polymer chains. The different fiber structures were ascribed to differences in the fiber
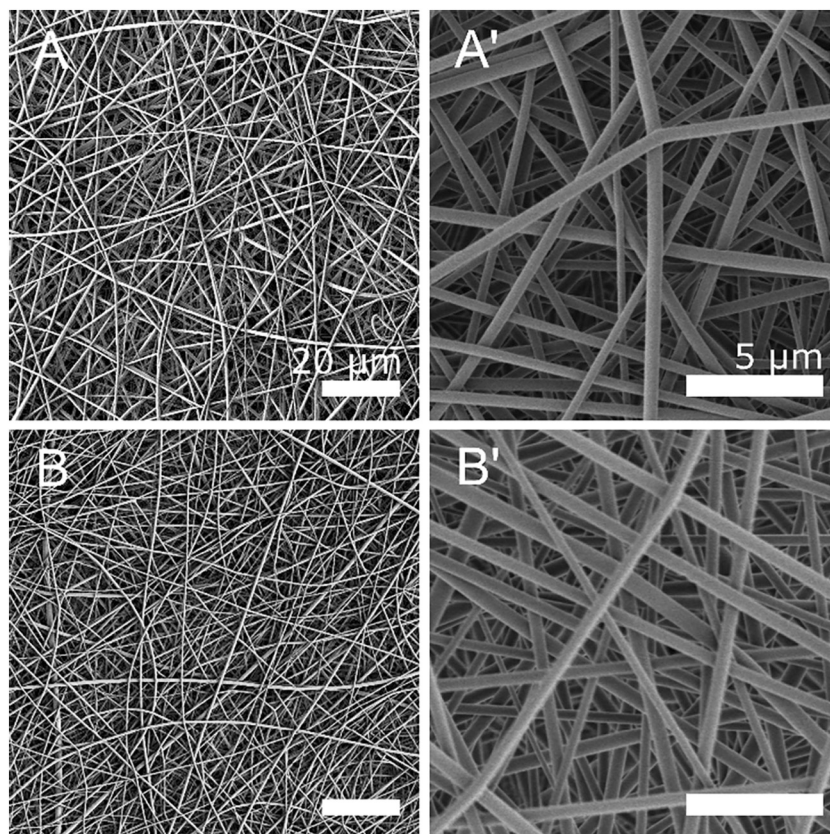
Fig. 2. SEM images of (A, A′) DCM90 and (B, B′) TFA100 as-spun membranes.
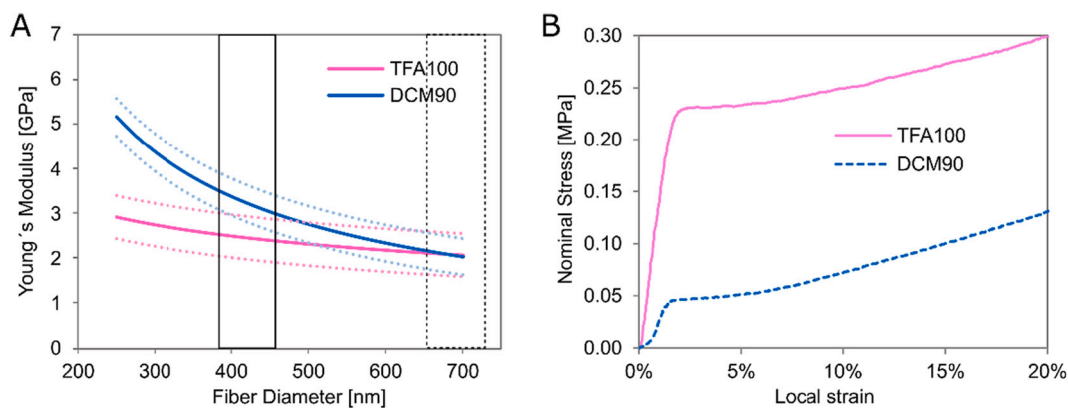

Fig. 3. (A) Power laws capturing the dependence of the Young's modulus of TFA100 and DCM90 single fibers in function of their diameter, adapted from previously published data and displayed for comparison [26]. The dashed lines represent the error between the measured data and the corresponding power law. The here reported DCMC90 or TFA100 membranes fall to the left on the x-axis (square, full line), displaying a mean diameter of 390 ± 90 nm or 460 ± 100 nm, respectively; DCM90+ or TFA100+ membranes towards the right (square, dashed line) with mean fiber diameters of 730 ± 190 or 650 ± 170, respectively. (B) Stress-strain curves obtained from uniaxial tensile experiments of DCM90 and TFA100 membranes.

formation process, in particular the evaporation rate and the water miscibility of the spinning solvents. The latter one influences the interactions with the ambient water vapor. The higher evaporation rate of DCM and its non-miscibility with water induces a rapid solidification of the jet during the electrospinning process. The solidified fiber is then further drawn by the high electrostatic fields inducing the formation of nanofibrils along the fiber axis which enhances the stiffness of obtained fibers. On the other hand, TFA has a lower vapor pressure and residual solvent molecules may remain in the fiber after deposition on the collector, what was for example observed for DMF, a solvent with low vapor pressure [50]. This scenario favors the relaxation of the

amorphous polymer chains within the fiber, resulting in fibers that exhibit lower Young's moduli than DCM90 fibers.

On the macroscopic level, the overall porosity ϕ and the fiber orientation are two of the most important factors determining the mechanical behavior of electrospun membranes [8,11,51]. DCM90 and TFA100 membranes showed no preferential fiber orientation. However, a slightly higher porosity value was found for the DCM90 sample compared to the TFA100 for similar sample thicknesses (Table 1). TFA100 membranes incorporated thus a more compact fiber network, with a fiber content ~50% higher than for DCM90 membranes, estimated based on the thickness, weight and area of the membrane in

Table 1

Characteristics of DCM90 and TFA100 membranes and corresponding mechanical properties.

Sample	Thickness t_m [μm]	Porosity ϕ [%][a]	Fiber content ν_F [%][a]	$P_{Y, m}$ [kPa]	E_m [MPa]	E_{m, ν_F} [MPa]
DCM90	169 ± 16	95.2 ± 0.5	4.8 ± 0.5	47 ± 4	5.4 ± 0.5	111 ± 10
TFA100	177 ± 19	92.5 ± 0.9	7.5 ± 0.9	220 ± 10	16.2 ± 0.9	215 ± 12

[a] Mean value ± error of propagation based on Eq. (4).

relation to the density of PLLA.

The mechanical properties of DCM90 and TFA100 membranes were compared in terms of Young's modulus E_m and yield stress $P_{Y, m}$ measured by uniaxial tensile testing. Resulting stress-strain curves are shown in Fig. 3B for both types of sample. Young's moduli and yield stresses were extracted and reported in Table 1. The TFA100 membrane had higher values for both parameters. There is thus a discrepancy between the mechanical properties measured at the fiber level and the one observed at the membrane level.

3.2. Fiber-to-fiber bonds

Beside the architecture of the network and the intrinsic properties of the underlying fibers, the presence of fiber-to-fiber bonds influences the overall mechanical properties of membranes such as the stiffness and the elongation at break [27]. In the context of this study, fiber-to-fiber bonds are defined as cross-points where superimposed fibers are physically bonded, due to residual solvent within the fibers during their deposition, rather than crossing points of dried fibers in the non-woven network. In previous studies [37,45], we demonstrated by numerical and experimental analyses the influence of such bonds on the deformation mechanism of the network. The density in fiber-to-fiber bonds, and thus the fiber segment length s_f between two bonds, was shown to affect the

mechanical behavior of the membranes, including auxetic behavior. Auxetics are materials with negative Poisson's ratio [52]. They expand in a direction perpendicular to the applied extension, and thus become wider or thicker upon stretching.

The pronounced auxetic behavior of selected electrospun membranes was explained by the lateral contraction of the membrane upon stretching, which induces out-of-plane buckling of the fibers initially oriented transversally to the stretching direction [37]. Since longer, more slender segments were associated with lower critical buckling loads and larger buckling amplitudes, they entailed larger increases in thickness and volume of the membrane. For this reason, taking into account the similar diameter of the fiber in the two membranes, the measured change in thickness of the membranes upon uniaxial stretching was used as an indirect measure of the length of fiber segments s_f, and hence the density in fiber-to-fiber bonds in the present work. A higher density in bonds implies shorter segments s_f, leading to a reduced auxetic behavior.

The increase in thickness of DCM90 and TFA100 membranes upon stretching was measured and compared to evaluate the qualitative difference in fiber segment length s_f between the two networks (Fig. 4A, B). When uniaxially stretched to 20%, the thickness of the TFA100 membranes increased by ~270% up to 480 ± 34 μm, while an increase of 640% (up to 1075 ± 58 μm) was observed for the DCM90 meshes. The bent buckled fibers in stretched DCM90 and TFA100 samples, which are typical for the underlying mechanism of the auxetic expansion [37], are shown and indicated by arrows in Fig. 4A′, B′. The less than halved increase in thickness indicates a lower aspect ratio of fiber segments in the TFA100 samples when compared to the DCM90 ones. Considering the only moderate difference in diameter this suggests shorter segments, i.e. lower s_f and thus a greater number of fiber-to-fiber bonds per volume unit of the TFA100 mesh (Table 1).
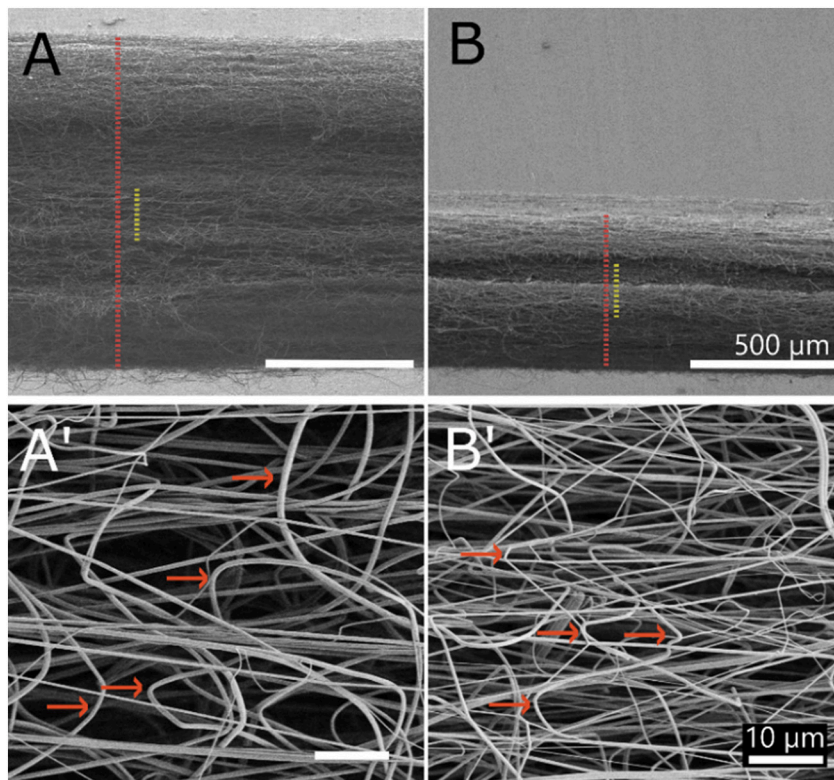
Fig. 4. Membrane deformation upon stretching to 20% strain. Cross-sectional view by SEM of (A) the DCM90 and (B) TFA100 membrane, and respective top-views (A′, B′). The red dashed line indicates the membrane thickness after stretching and the yellow dashed line the initial thickness. The membranes were stretched in the horizontal direction (↔) in all pictures. The arrows indicate buckling fibers. (For interpretation of the references to colour in this figure legend, the reader is referred to the web version of this article.)

3.3. Effects of spinning solution on multiscale properties of fibrous membranes

Spinning parameters were adapted in order to minimize the architectural differences among the membranes, particularly reaching comparable fiber diameters. Therewith, the focus was put on the differences in mechanical properties and the nature of fiber-to-fiber interactions at their crossing points. The most striking observation is the discrepancy between the lower Young's modulus of TFA100 single fibers, but the higher stiffness of the respective membrane compared to DCM90 samples. This outcome results from the use of TFA, which has a lower evaporation rate than DCM. This was also simulated using Hansen Solubility Parameters in Practice (HSPiP) (http://www.hansen-solubility.com/) and displayed in Fig. S1. When reaching the collector, TFA100 fibers contain more residual solvents. They are thus heavier and carry more charges, leading to a higher kinetic energy at the time of deposition. We hypothesize that these conditions have three main consequences. First, it allows the relaxation of polymer chains after deposition, thereby decreasing the fiber's Young's modulus [26]. Secondly, due to their higher kinetic energy and lower stiffness, the fibers bend/sink into the pores formed by the previously deposited fibers during landing and thus decrease the overall porosity ϕ. Finally, wet fibers with higher kinetic energy (i.e. TFA100) will more likely form welded fiber-to-fiber bonds resulting in a more compact network. This promotes a higher level of cooperation between the fibers to resist membrane deformation.

To demonstrate the influence of fiber-to-fiber bonds to the macroscopic mechanical properties of the network, the membrane's Young's moduli were normalized to the respective fiber content per volume ν_F. Nevertheless, the TFA100 membranes still exhibit higher values in normalized Young's modulus $E_{m, \nu F}$ (Table 1). Thus, the difference in porosity ϕ, per se, does not explain the differences in mechanical properties of an electrospun membrane. In summary, two electrospun membranes, DCM90 and TFA100, were investigated on the microscopic, single fiber level, as well as on the macroscopic, whole membrane level. Results revealed that the persistence length l_p and fiber diameter were comparable in both membranes, while the Young's modulus E_f of individual fibers was increased in DCM90 compared to TFA100. Fiber-to-fiber bonds and overall fiber content were decreased in DCM90 compared to TFA100, giving this membrane an overall lower Young's modulus E_m compared to TFA100.

3.4. Cell viability on PLLA membranes

The importance of micro- meso-, or macroscale properties of electrospun membranes on cell fate and tissue development has been previously described [34,53] based on the distinct interplay between single fibers and single cells, and bulk membranes with tissues. At the microscale, highly heterogeneous deformations upon planar biaxial stretching were observed, partially based on fiber crossing points and tortuosity, while at the macroscale, homogeneous deformation was reported. Concomitantly, it is important to understand and control the local fibrous environment to understand cell responses to mechanical deformations of entire constructs. To this end, we evaluated as spun membranes with distinct fiber-to-fiber bonds in vitro and investigated how cell permissive the respective membranes were.

Prior to cell migration experiments, we assessed whether membranes produced under different conditions, DCM90 or TFA100, would induce changes in the metabolic activity of fibroblasts. Cell viability assays were performed on day 1, 4 and 7 post seeding. The relative metabolic activity is displayed in Fig. 5. On both membranes, cell metabolic activity increased over time, with significant differences between day 7 and day 1 in both conditions. When comparing the cell metabolic activity between the two membranes, DCM90 and TFA100, on each respective day, no significant differences were observed.

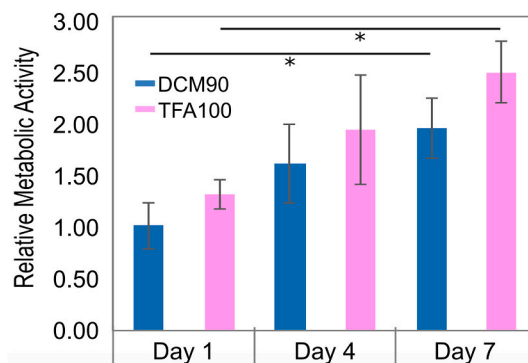The increase in cell metabolic activity can be explained by cell

Fig. 5. Cell metabolic activity quantified by alamarBlue assays (* = $p < 0.05$). Over time, an increased metabolic activity was observed which is indicative for cell proliferation on the membranes.

proliferation over time, and thus an overall increase in cell number. SEM images and fluorescent images obtained after 1- or 4-days post seeding further support this thesis. As presented in Fig. 6, an increase in cell coverage from day 1 to day 4 can be observed on both membranes. One day after seeding, NHDF formed cell aggregates on both membranes with preferred cell-cell contacts than cell-material contacts. After 4 days, however, NHDF spread on the membranes and formed a monolayer that covered large areas of the scaffold. The initial aggregate formation can be related to an insufficient wetting of the highly hydrophobic PLLA membranes upon cell seeding [54,55]. Over time, cells secrete their own extracellular matrix, proteins are adsorbed on the membranes, which subsequently provide a better interface for cells to adhere. Based on alamarBlue assays and microscopy images, we can conclude that electrospun PLLA membranes are cytocompatible in the here used in vitro setting and that DCM90 or TFA100 do not induce distinct cell responses. Furthermore, these data indicate that the membranes are suitable for cell culture, irrespective of the solvent used.

3.5. Cell infiltration and migration through PLLA membranes

A limitation of electrospun membranes, produced by conventional e-spinning set-ups, concerns the relatively small pore size, which restricts cellular infiltration and 3D tissue formation. Moreover, the fiber network acts as a diffusion barrier, lowering nutrients availability within the membrane [56]. A variety of techniques have been developed to increase the pores of electrospun membranes, among them the use of sacrificial particles or fibers, or postprocessing methods by laser ablation [57]. In addition to these efforts, simultaneous electrospinning and cell electrospraying was exploited to embed cells within fibrous networks [32]. In their work, the authors report changes in the mechanical response at the macro scale based on modulated fiber interconnections but did not investigate cell migration through these networks. To the best of our knowledge, the effect of fiber-to-fiber bonds on cell migration through electrospun membranes has not been addressed to date.

As summarized under 3.3, we deduced that the choice in solvent system (DCM or TFA) induced a significant change in the nature of fiber-to-fiber interactions: TFA100 membranes incorporated indeed more fiber-to-fiber bonds, resulting in an overall more compact network, reducing the chances for fiber rearrangement in cell culture. We therefore compared the two membranes, produced from TFA or DCM, to investigate whether the presence or absence of fiber-to-fiber bonds affects lateral cell migration. To this end, a cell sandwich experiment was developed to investigate cellular infiltration through an electrospun scaffold in function of its architecture, mechanical properties, and fiber-to-fiber bonds (Fig. 1). In this experimental setup, the cells are lying between two membranes. We hypothesize that the superimposed membrane II forms a barrier towards nutrients in fresh cell culture medium and oxygen, thereby reducing the availability of these
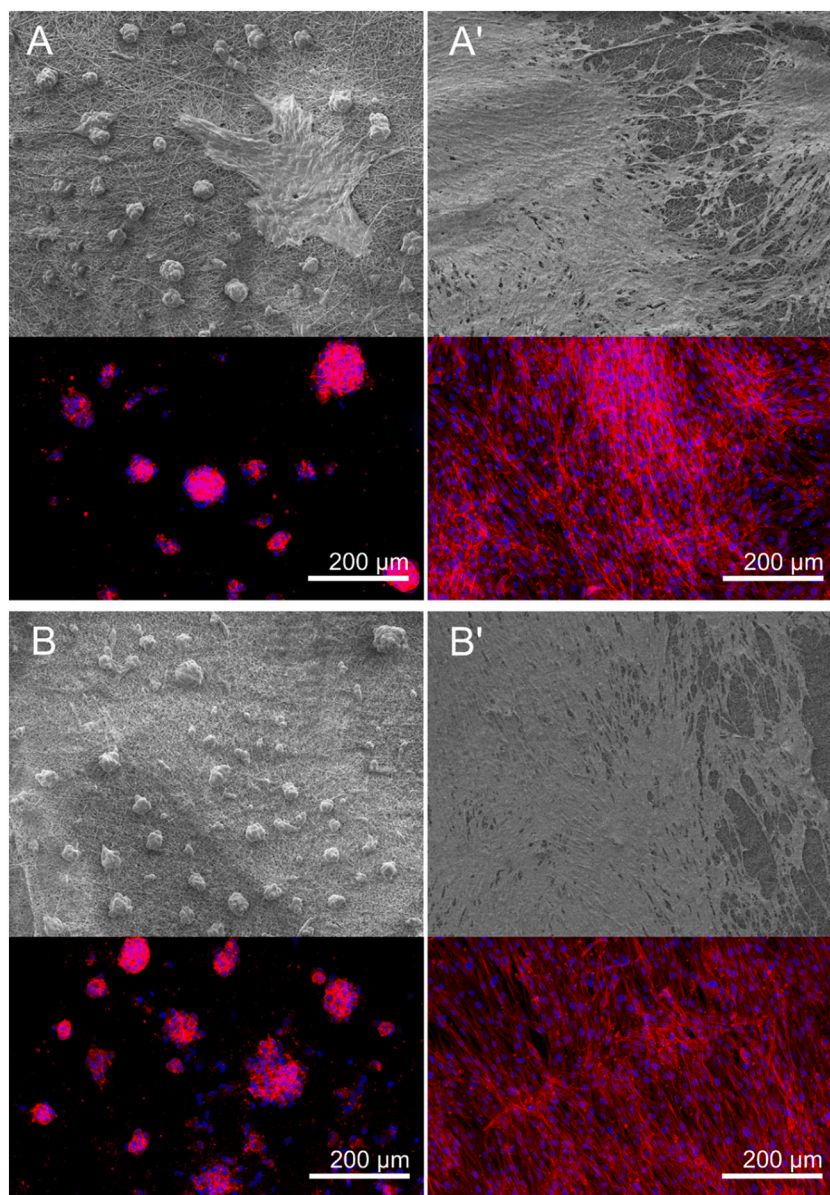
Fig. 6. SEM and fluorescent images of NHDF cultured on different PLLA electrospun scaffolds. Actin skeleton is stained in red, nuclei in blue. (Top) NHDF on DCM90 membranes on day 1 (A) and 4 (A′). (Bottom) NHDF on TFA100 membranes on day 1 (B), and 4 (B′). (For interpretation of the references to colour in this figure legend, the reader is referred to the web version of this article.)

important factors to the cells. As a consequence, a gradient is formed across the membrane, with an accumulation of metabolic waste products and reduced nutrients around the cells within the sandwich. This is suggested to trigger cell migration through the membrane towards fresh cell culture medium. In this way, we assessed cell migration by quantifying the area covered by cells on top of the membrane *II*.

Quantifying and measuring cell migration is a highly complex scenario, influenced by a multitude of factors which was not investigated in this paper. In our simplified in vitro model, NHDF migration through the membranes was hypothesized to occur along the nutrient gradient, towards fresh culture medium. Comparing two different membranes, DCM90 and TFA100, in an identical cell culture scenario allowed us to draw conclusions on the respective cell migration and influencing factors of the used scaffolds. Displayed in Fig. 7, we observed that neither DCM90 nor TFA100 membranes permitted cell migration, indicated by the absence of cells on the top membrane. This was to be expected based on the small fiber diameter and resulting pore size of <5 μm (Table S1). Nevertheless, the interesting differences in fiber-to-fiber bonds despite

their very similar visual architecture (Fig. 2) warranted in vitro analysis.

To further investigate our hypothesis of increased cell migration through membranes of loose fiber-to-fiber bonds, two additional membranes, DCM90+ and TFA100+, were developed with the aim of favoring cell infiltration through increased fiber diameters and resulting pore sizes of >5 μm. These membranes were produced by increasing the polymer concentration of respective DCM90 and TFA100 electrospinning solutions. The resulting fiber diameter, membrane thickness, porosity and apparent pore size are reported in Table 2. The lower porosity of membranes composed of thicker fibers (i.e. DCM90+ and TFA100+ compared to their homologues) might be explained by their higher mass. Interestingly, the difference in porosity ϕ between DCM90+ and TFA100+ is lower than between DCM90 and TFA100. Accordingly, the fiber stiffness is expected to be similar for both DCM90+ and TFA100+ membranes according to Fig. 3A.

The pore sizes were compared to the different membranes based on SEM images (Fig. 8). It is delicate to objectively define a pore in a 3-dimensional fibrous network. Only pores with a more obvious
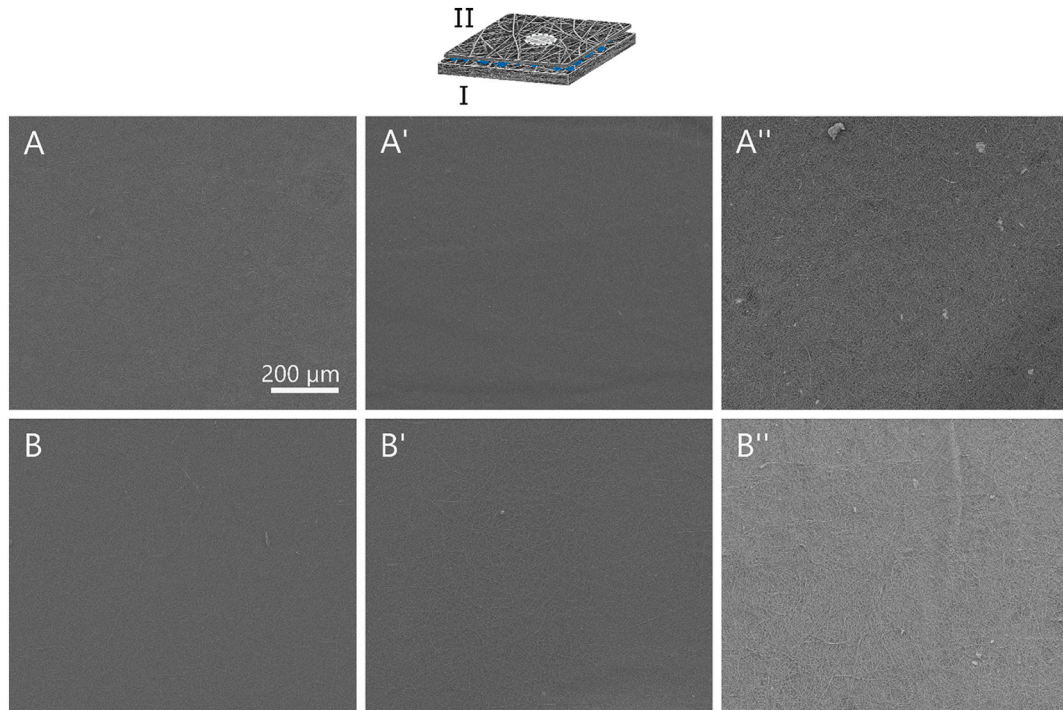
Fig. 7. Cell-sandwich experiments with DCM90 (A) and TFA100 (B) membranes. (Top) Sketch of the setup; bottom membrane *I*, on which cells (blue) are seeded, and top membrane *II*. (Bottom) Cell infiltration is evaluated by observing the top surface of the membrane *II* at different time points. SEM images of (A) DCM90 and (B) TFA100 samples after 4 (A,B), 11 (A′,B′) or 18 days (A″,B″) of incubation. (For interpretation of the references to colour in this figure legend, the reader is referred to the web version of this article.)

Table 2
Characteristics of TFA100+ and DCM90+ samples used as membrane II for the sandwich experiments.

| Sample	Fiber diameter d_f [nm]	Thickness t_m [µm]	Porosity ϕ [%][a]	Fiber content ν_F [%][a]	Pore size [µm^2]
DCM90+	730 ± 190	60 ± 5	93.3 ± 0.6	6.7 ± 0.6	6.9 ± 1.8
TFA100+	650 ± 170	73 ± 7	91.8 ± 0.8	8.2 ± 0.8	4.9 ± 1.9

[a] Mean value ± error of propagation based on Eq. (4).

deepness were considered as described in Section 2.3. Overall, the measured pore dimensions are quite small compared to the cell diameter (>10 µm) to allow cell migration (Table 2). However, the network architecture is complex, out-of-plane pore interconnectivity cannot be measured from 2D-images but significantly contributes to the overall accessible pore. The real 3-dimensional pore sizes should thus be higher than our values. As expected, bigger pore sizes were found for membranes incorporating thicker fibers [58].

As shown in top views of DCM90+ and TFA100+ sandwich constructs after different days of incubation (Fig. 9A and B), a few NHDFs could already reach the top of DCM90+ membrane *II* on day 11 and were covering 28% ± 19% of the membrane surface on day 18. Importantly, cells were also localized within the fiber network. A closer look from the top of the membrane and the cross-section imaging of DCM90+ membrane *II* provide evidence for the presence of cells within the network (Fig. 10). On the other side, lower cell infiltration was measured for TFA100+ (Fig. 9), as cells could only be observed on day 18, covering on average less than 3%. The TFA100+ sample with the highest cell coverage reached a value of 7% ±2%. This is in agreement with our initial hypothesis that cell permissive networks can be developed by steering fiber-to-fiber bonds.
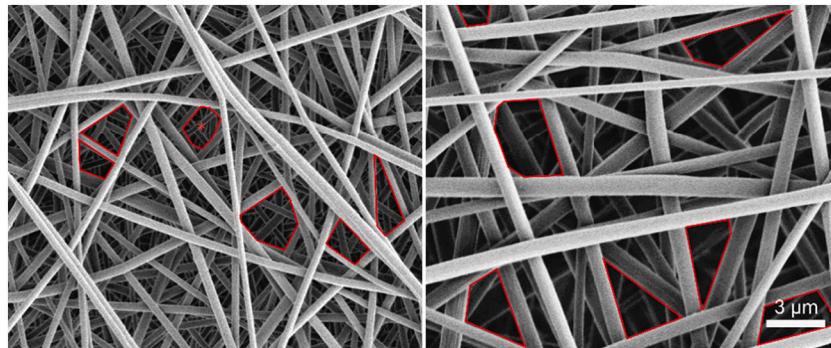
Fig. 8. SEM images of DCM90 (left) and DCM90+ (right) membranes demonstrating the difference in pore size (manually outlined in red). The (*) indicates a pore whose delimiting fibers are not all on the same level. (For interpretation of the references to colour in this figure legend, the reader is referred to the web version of this article.)
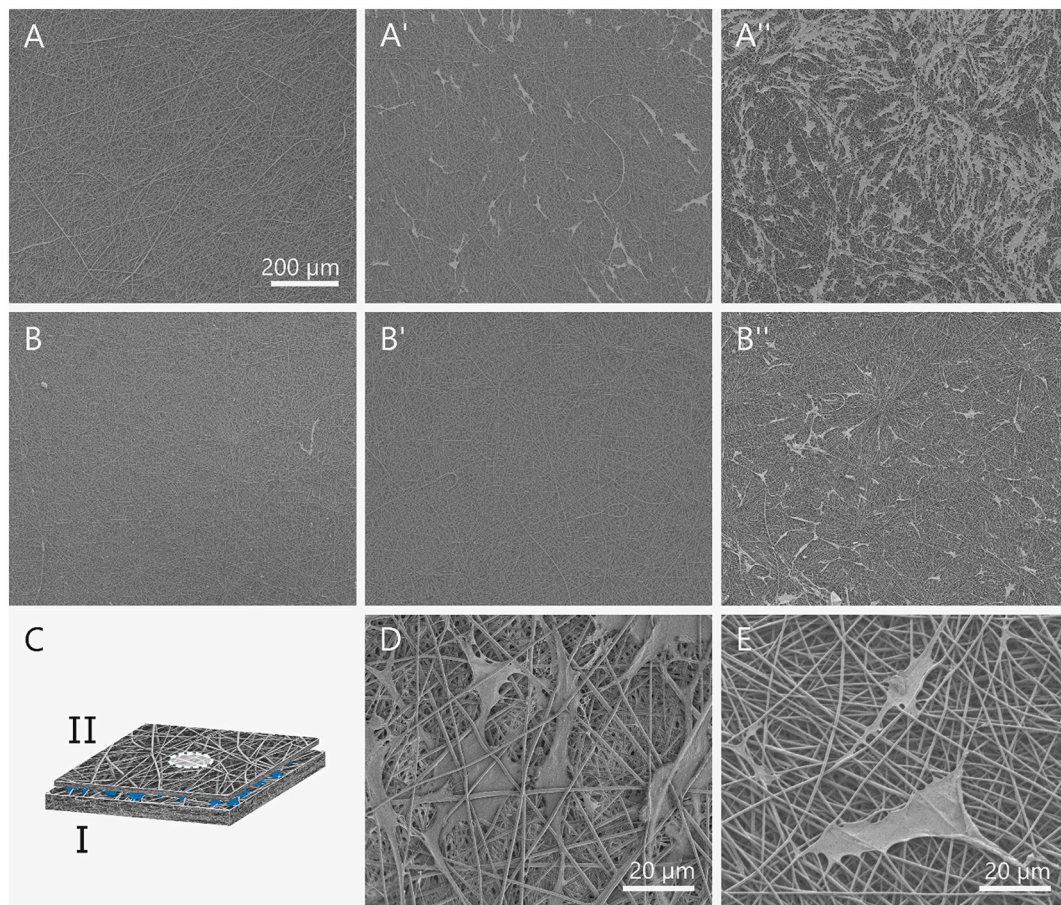
Fig. 9. Cell sandwich experiments. Cell infiltration is evaluated by observing the top surface of the membrane *II* at different time points. SEM images of (A) DCM90+ and (B) TFA100+ samples on day 4 (A,B), 11 (A′,B′) and 18 (A″,B″) after seeding. (C) Sketch of the setup; bottom membrane *I*, on which cells (blue) are seeded, and top membrane *II*. (D) and (E) images of higher magnification displaying cells migrated through DCM90+ or TFA100+ membranes after 18 days. (For interpretation of the references to colour in this figure legend, the reader is referred to the web version of this article.)
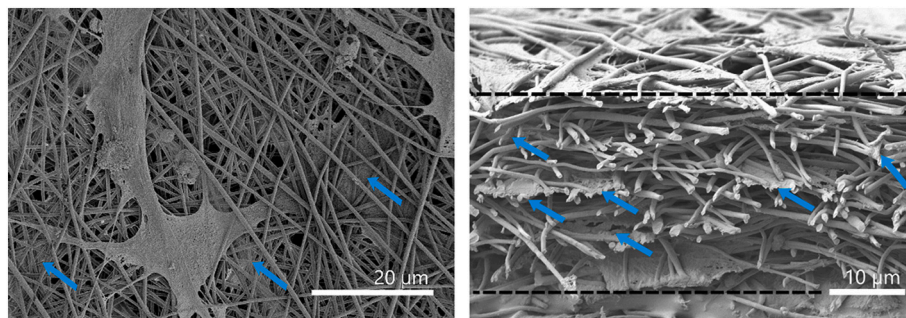
Fig. 10. SEM images showing cell infiltration and migration through DCM90+ membranes. (A) Membrane top view on day 11. (B) Cross-section view of DCM90+ membrane *II* after 20 days of cell culture. Blue arrows indicate cells within the fiber network. (For interpretation of the references to colour in this figure legend, the reader is referred to the web version of this article.)

The results demonstrate that a change in fiber diameter significantly influences cell infiltration, since no cell migration through the membrane was visible for DCM90 and TFA100 samples, although these membranes were thinner [57]. In our case, the fiber diameter threshold for cell infiltration must be between the diameter of TFA100 (460 nm) and TFA100+ (650 nm). Of note, however, in most studies cells were exclusively seeded under static conditions on top of the membranes, with migration towards the inside of the scaffold against a potential nutrient gradient. In our sandwich approach, cell migration through the membrane was investigated from bottom to top in response to an increased nutrient concentration. By this, we could create a model where cell culture medium served as a chemoattractant to stimulate cell migration.

According to the cell viability results, it is obvious that the reduced cell migration through TFA100+ membranes compared to DCM90+ is not due to reduced viability or proliferation on membranes produced from TFA solvent. To this end, our observations on cell infiltration can only be explained by the differences in network architectures and/or mechanical properties between the two types of membranes. In this respect, scaffolds produced from TFA solvents are mechanically more

compact, i.e. more fiber-to-fiber bonds, and the force required to move a fiber in this scaffold is higher than the ones derived from DCM solutions due to the short fiber segments s_f, a parameter considered to greatly influence the microscopic stiffness sensed by the cell [49]. The cells capacity to move through the membrane may thus be favored by the looser fiber network of DCM90+ [59]. However, we cannot exclude the effects of the slightly higher porosity and pore sizes of DCM90+ membranes that may also facilitate the cell migration. Tailoring architectural properties, i.e. fiber diameter and pore sizes, of electrospun membranes individually is not possible, due to their direct interdependency. Cell migration and scaffold infiltration is thus dependent on the interplay between pore size and fiber diameter.

Further work may investigate the potential of pre-stretched membranes that show strong auxetic behaviors for cell infiltration. As shown for stretched DCM90 samples (Fig. 4A), such scaffolds exhibit a drastic increase in volume, and thus increased porosity, which may promote cell invasion within the network. Preliminary experiments were already performed by seeding fibroblasts on top of such pre-stretched membranes. After 3 days only, a portion of cells were already found underneath the first layers of fibers (Supp. Fig. S2).

4. Conclusions

The characterization of electrospun membranes from the nano- to the macroscale, in terms of architecture and mechanical properties, revealed that membranes produced from TFA solutions contained a higher density of fiber-to-fiber bonds than those produced from DCM/ DMF blend solutions. The forces are more efficiently transmitted between the fibers, favoring a stiffer response to stretching deformation and overcoming the mechanical contribution related to the single fiber's Young's modulus. Since the number of fiber-to-fiber bonds influences the force needed to move or deform a single fiber segment in a network, it may also influence the ability of cells to mechanically act on the substrate, generating voids, and thus to infiltrate and migrate through a scaffold. To this end, it was hypothesized that a compact membrane such as the TFA100 and TFA100+ meshes may be perceived as an immovable barrier. The hypothesis was investigated by developing an approach to assess the cell infiltration and migration. A cell sandwich setup was designed, where cells are comprised between two electrospun membranes, encouraging cells to migrate through the mesh to access the nutrients present in the cell culture medium. A higher cell infiltration was observed for DCM90+ scaffolds compared to TFA100+, suggesting that membranes with looser fibers, that are easier to move and deform, can promote the formation of 3D tissues. These experiments revealed also that a threshold in fiber diameter, found between 400 nm to 700 nm, dictates whether NHDF can infiltrate the PLLA network or not.

In general, we would like to emphasize the importance of fiber-to-fiber bonds on cell mobility and help future research to further elucidate the principles behind cell migration within electrospun membranes. Crucial effects of local cell-fiber interactions and mechanical properties on the micro-scale to address tissue formation or regeneration cannot be overemphasized and future work should take differences on distinct length scales into account. While electrospinning is a versatile method to produce fibrous membranes of distinct chemical, physical and mechanical properties, highly complex mechanisms and interdependent parameters during the spinning process render the control over isolated characteristics challenging if not impossible. To this end, changes in fiber diameters are ultimately associated with changes in mechanical properties, and changes in spinning solution formulations necessitate e. g. altered voltage. Our work thus encounters certain limitations in that changes in fiber-to-fiber bonds come along with alterations in fiber diameter. Cell migration, or cell fate in general, is thereby not only governed by isolated parameters, but overall characteristics of the specific membranes. Furthermore, technical limitations such as instruments operating in high vacuum, did not allow to study fiber buckling under wet, physiological conditions. While of little relevance for the current

study, in which the resulting auxetic effect was analyzed in air and used as an indirect qualitative measure of segment length and density of bonds, it would be interesting to achieve such evaluations in the future to gain in depth understanding of cell-material interactions under physiological loads and conditions and to establish representative in vitro models.

Altogether, our results link the microscopic and macroscopic mechanical properties of electrospun membranes to cell fate and provide new insight into the development of electrospun scaffolds for tissue engineering application. With our approach, the use of specific electrospinning setups (e.g. cryogenic), sacrificial micron-scaled fibers or the use of sophisticated cell migration assays with chemo-attractants is not needed.

CRediT authorship contribution statement

Alexandre Morel: Conceptualization, Formal analysis, Investigation, Methodology, Writing – original draft. **Anne Géraldine Guex:** Conceptualization, Formal analysis, Investigation, Methodology, Writing – original draft. **Fabian Itel:** Investigation, Writing – review & editing. **Sebastian Domaschke:** Investigation, Writing – review & editing. **Alexander E. Ehret:** Writing – review & editing. **Stephen J. Ferguson:** Supervision, Writing – review & editing. **Giuseppino Fortunato:** Conceptualization, Supervision, Writing – review & editing. **René M. Rossi:** Funding acquisition, Resources, Supervision, Writing – review & editing.

Declaration of competing interest

The authors declare no competing financial interest.

Appendix A. Supplementary data

Supplementary data to this article can be found online at https://doi.org/10.1016/j.msec.2021.112427.

References

[1] J. Yin, S. Luan, Regen. Biomater. 3 (2016) 129–135.
[2] S. Bose, M. Roy, A. Bandyopadhyay, Trends Biotechnol. 30 (2012) 546–554.
[3] F. Groeber, M. Holeiter, M. Hampel, S. Hinderer, K. Schenke-Layland, Clin. Plast. Surg. 39 (2012) 33–58.
[4] A. Hasan, A. Memic, N. Annabi, M. Hossain, A. Paul, M.R. Dokmeci, F. Dehghani, A. Khademhosseini, Acta Biomater. 10 (2014) 11–25.
[5] M. Jafari, Z. Paknejad, M.R. Rad, S.R. Motamedian, M.J. Eghbal, N. Nadjmi, A. Khojasteh, J. Biomed. Mater. Res. B Appl. Biomater. 105 (2017) 431–459.
[6] Q.P. Pham, U. Sharma, A.G. Mikos, Tissue Eng. 0 (2006), 060509065116001.
[7] J. Xue, T. Wu, Y. Dai, Y. Xia, Chem. Rev. 119 (2019) 5298–5415.
[8] J. Voorneveld, A. Oosthuysen, T. Franz, P. Zilla, D. Bezuidenhout, J. Biomed. Mater. Res. B Appl. Biomater. (2016) 1–14.
[9] D. G. Han, C. B. Ahn, J. H. Lee, Y. Hwang, J. H. Kim, K. Y. Park, J. W. Lee and K. H. Son, Polymers (Basel), DOI:https://doi.org/10.3390/polym11040643.
[10] Y.M. Ju, J.S. Choi, A. Atala, J.J. Yoo, S.J. Lee, Biomaterials 31 (2010) 4313–4321.
[11] B.M. Baker, A.O. Gee, R.B. Metter, A.S. Nathan, R.A. Marklein, J.A. Burdick, R. L. Mauck, Biomaterials 29 (2008) 2348–2358.
[12] A.P. Kishan, E.M. Cosgriff-Hernandez, J. Biomed. Mater. Res. A 105 (2017) 2892–2905.
[13] M.F. Leong, M.Z. Rasheed, T.C. Lim, K.S. Chian, J. Biomed. Mater. Res. A 91 (2009) 231–240.

[14] O. L. A. Harrysson, O. Cansizoglu, D. J. Marcellin-little, D. R. Cormier and H. A. West, 2008, 28, 366–373.

[15] Y. Hong, A. Huber, K. Takanari, N.J. Amoroso, R. Hashizume, S.F. Badylak, W. R. Wagner, Biomaterials 32 (2011) 3387–3394.

[16] F.M. Watt, W.T.S. Huck, Nat. Rev. Mol. Cell Biol. 14 (2013) 467–473.

[17] I.V. Andrianov, A.I. Manevich, Y.V. Mikhlin, O.V. Gendelman, Problems of Nonlinear Mechanics and Physics of Materials, 2019.

[18] K. Ghosal, A. Chandra, G. Praveen, S. Snigdha, S. Roy, C. Agatemor, S. Thomas, I. Provaznik, Sci. Rep. 8 (2018) 1–9.

[19] B.M. Baker, B. Trappmann, W.Y. Wang, M.S. Sakar, I.L. Kim, V.B. Shenoy, J. A. Burdick, C.S. Chen, Nat. Mater. 14 (2015) 1262–1268.

[20] A. Morel, S. Domaschke, V. Urundolil Kumaran, D. Alexeev, A. Sadeghpour, S. N. Ramakrishna, S.J. Ferguson, R.M. Rossi, E. Mazza, A.E. Ehret, G. Fortunato, Acta Biomater. 81 (2018) 169–183.

[21] B. Janković, J. Pelipenko, M. Škarabot, I. Muševič, J. Kristl, Int. J. Pharm. 455 (2013) 338–347.

[22] A. Arinstein, M. Burman, O. Gendelman, E. Zussman, Nat. Nanotechnol. 2 (2007) 59–62.

[23] F. Croisier, A.S. Duwez, C. Jérôme, A.F. Léonard, K.O. Van Der Werf, P.J. Dijkstra, M.L. Bennink, Acta Biomater. 8 (2012) 218–224.

[24] C.T. Lim, E.P.S. Tan, S.Y. Ng, Appl. Phys. Lett. 92 (2008) 141908.

[25] G. Yazgan, R.I. Dmitriev, V. Tyagi, J. Jenkins, M. Rottmar, R.M. Rossi, C. Toncelli, D.B. Papkovsky, K. Maniura-weber, G. Fortunato, Sci. Rep. (2017) 1–13.

[26] A. Morel, S.C. Oberle, S. Ulrich, G. Yazgan, F. Spano, S.J. Ferguson, Nanoscale 11 (2019) 16788–16800.

[27] H. Li, C. Zhu, J. Xue, Q. Ke, Y. Xia, Macromol. Rapid Commun. 38 (2017) 1–5.

[28] H. Maleki, A. A. Gharehaghaji, L. Moroni and P. J. Dijkstra, Biofabrication, DOI: https://doi.org/10.1088/1758-5082/5/3/035014.

[29] K. Yoon, B.S. Hsiao, B. Chu, Polymer (Guildf). 50 (2009) 2893–2899.

[30] U. Stachewicz, F. Hang, A.H. Barber, Langmuir 30 (2014) 6819–6825.

[31] Q. Shi, K.T. Wan, S.C. Wong, P. Chen, T.A. Blackledge, Langmuir 26 (2010) 14188–14193.

[32] N.J. Amoroso, A. D'Amore, Y. Hong, W.R. Wagner, M.S. Sacks, Adv. Mater. 23 (2011) 106–111.

[33] A. D'Amore, N. Amoroso, R. Gottardi, C. Hobson, C. Carruthers, S. Watkins, W. R. Wagner, M.S. Sacks, J. Mech. Behav. Biomed. Mater. 39 (2014) 146–161.

[34] J.A. Stella, W.R. Wagner, M.S. Sacks, J. Biomed. Mater. Res. A 93 (2010) 1032–1042.

[35] P. Saini, M. Arora, M.N.V.R. Kumar, Adv. Drug Deliv. Rev. 107 (2016) 47–59.

[36] J.S. Bergström, D. Hayman, Ann. Biomed. Eng. 44 (2016) 330–340.

[37] S. Domaschke, A. Morel, G. Fortunato, A.E. Ehret, Nat. Commun. 10 (2019) 4863.

[38] C.A. Schneider, W.S. Rasband, K.W. Eliceiri, Nat. Methods 9 (2012) 671–675.

[39] R.W. Ogden, G. Saccomandi, I. Sgura, Proc. R. Soc. A Math. Phys. Eng. Sci. 462 (2006) 749–768.

[40] G. Lamour, J.B. Kirkegaard, H. Li, T.P.J. Knowles, J. Gsponer, Source Code Biol. Med. 9 (2014) 1–6.

[41] C. Rivetti, M. Guthold, C. Bustamante, J. Mol. Biol. 264 (1996) 919–932.

[42] D. Garlotta, J. Polym. Environ. 9 (2002) 63–84.

[43] M.K. Selatile, S.S. Ray, V. Ojijo, R. Sadiku, Fibers Polym. 20 (2019) 100–112.

[44] X. Zhu, W. Cui, X. Li, Y. Jin, Biomacromolecules 9 (2008) 1795–1801.

[45] S. Domaschke, A. Morel, R. Kaufmann, J. Hofmann, R. M. Rossi, E. Mazza, G. Fortunato and A. E. Ehret, J. Mech. Behav. Biomed. Mater., DOI:https://doi.org/10.1016/j.jmbbm.2020.103634.

[46] A.G. Guex, G. Fortunato, D. Hegeman, H.T. Tevaearai, M.-N. Giraud, General Protocol for the Culture of Cells on Plasma-coated Electrospun Scaffolds vol. 1058, 2013.

[47] C.L. Pai, M.C. Boyce, G.C. Rutledge, Polymer (Guildf). 52 (2011) 6126–6133.

[48] R.C. Picu, Soft Matter 7 (2011) 6768.

[49] M. Zündel, A.E. Ehret, E. Mazza, Acta Biomater. 84 (2019) 146–158.

[50] L. Weidenbacher, A. Abrishamkar, M. Rottmar, A.G. Guex, K. Maniura-Weber, A. J. deMello, S.J. Ferguson, R.M. Rossi, G. Fortunato, Acta Biomater. 64 (2017) 137–147.

[51] G.H. Kim, Biomed. Mater. 3 (2008), 025010.

[52] K.E. Evans, M.A. Nkansah, I.J. Hutchinson, S. Rogers, Nature 353 (1991) 10065.

[53] J.A. Stella, J. Liao, Y. Hong, W. David Merryman, W.R. Wagner, M.S. Sacks, Biomaterials 29 (2008) 3228–3236.

[54] S. Chen, Y. Hao, W. Cui, J. Chang, Y. Zhou, J. Mater. Sci. 48 (2013) 6567–6577.

[55] L. Ren, V. Pandit, J. Elkin, T. Denman, J.A. Cooper, S.P. Kotha, Nanoscale 5 (2013) 2337–2345.

[56] N. Wang, K. Burugapalli, W. Song, J. Halls, F. Moussy, Y. Zheng, Y. Ma, Z. Wu, K. Li, J. Membr. Sci. 427 (2013) 207–217.

[57] J. Wu, Y. Hong, Bioact. Mater. 1 (2016) 56–64.

[58] J.L. Lowery, N. Datta, G.C. Rutledge, Biomaterials 31 (2010) 491–504.

[59] W.J. Li, C.T. Laurencin, E.J. Caterson, R.S. Tuan, F.K. Ko, J. Biomed. Mater. Res. 60 (2002) 613–621.